DEM SIMULATIONS OF PARTICLE DYNAMICS IN A SPHERONIZATION PROCESS TO DESCRIBE THE PELLETIZATION MECHANISMS

D. WEIS[1], D. THAETE[2], M. THOMMES[2], S. ANTONYUK[1]

[1] Chair of Particle Process Engineering, University of Kaiserslautern
Gottlieb-Daimler-Straße 44, 67663 Kaiserslautern, Germany
dominik.weis@mv.uni-kl.de, mvt.mv.uni-kl.de

[2] Chair of Solids Process Engineering, Technical University Dortmund
Emil-Figge-Street 68, 44227 Dortmund, Germany
dennis.thaete@bci.tu-dortmund.de, fsv.bci.tu-dortmund.de

Key words: Pharmaceutical Pellets, Spheronization, DEM, PIV

Abstract. Spheronization is an important process to produce pharmaceutical pellets with a narrow particle size distribution and a homogeneous outer particle surface. Thereby, cylindrical extrudates are rounded by different pelletization mechanisms [1]. These mechanisms are highly dependent on the particle dynamics in the spheronizer. Discrete Element Method simulations of the particle motions in a spheronizer were performed to study the particle dynamics. The elastic-plastic contact model used in the simulations was calibrated by experiments with spheronized pellets. The influence of different process conditions and particle properties on the particle kinematics and interactions was analyzed. Also a comparison of the simulation results with PIV measurements was performed.

1 INTRODUCTION

Pharmaceutical pellets are spherical granules with a narrow particle size distribution and a reproducible outer particle surface. Extrusion and spheronization is a common technique to produce such pellets. A spheronizer consists of a static cylindrical wall and a rotating disk with a structured surface (friction plate) as shown in Figure 1. Cylindrical extrudates are placed on the friction plate and are rounded during the spheronization process by different formation mechanisms [1].
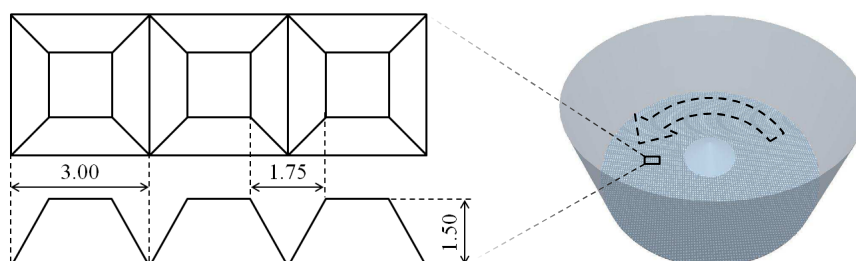

Figure 1: Schematic representation of the spheronizer (right) and the friction plate viewed from top (left top) and side (left bottom), (dimensions in mm) [2]

Describing the spheronization process is complex because these formation mechanisms take place simultaneously and are highly dependent on the particle dynamic, which is influenced by process conditions and particle properties. Therefore simulations can be helpful to predict the formation mechanisms. With Discrete Element Method (DEM) simulations the particle dynamics can be analyzed. Bouffard et al. have simulated the particle dynamics in the spheronizer using DEM to describe the segregation during spheronization of a bimodal particle system [3]. Koester et al. have performed DEM simulations of the movement of γ-Al_2O_3 particles in a spheronizer and have compared the results with PIV measurements [4].

The focus of the performed study was on the collision rate and collision forces of the particles, besides the particle motion. Various factors which influence the particle kinematic and collision characteristics were examined. In addition to process conditions like the rotational speed of the friction plate and the mass of particles in the spheronizer (loading) some properties of the particles like diameter, stiffness, coefficient of restitution and coefficient of static friction were varied. Also the obtained simulation results were compared with PIV measurements of the spheronization process of MCC pellets in [5].

To consider the particle-particle and particle-wall interactions in the DEM simulations, an elastic-plastic contact model was used because of the dominantly plastic behavior of the investigated pellets. The parameters of the contact model were calibrated by comparison with the performed single particle tests with spheronized pellets.

2 MATERIALS AND METHODS

2.1 Experimental Setup

The material parameters for the contact model of the DEM were determined by different uniaxial compression tests of pellets performed with the Texture Analyzer (TA.XTplus, Stable Micro Systems, UK). The pellets consist of 20 % (w) microcrystalline cellulose (MCC 102G SANAQ, Pharmatrans Sanaq, Switzerland) and 80 % (w) of α-lactose monohydrate (Granulac 200, Meggle, Germany) and are spheronized in a lab scale spheronizer (Schlueter RM300, Schlueter, Germany) [5]. Afterwards they are loaded up to a defined force or strain, while the force and the displacement are continuously recorded (see Figure 2). From these force displacement curves, different material parameters like compression strength, breakage force, stiffness and equivalent coefficient of restitution could be derived. Table 1 shows the results for pellets extruded with a water dosage rate of 15.5 g/min which have a diameter of $d_p = 1 - 3$ mm.
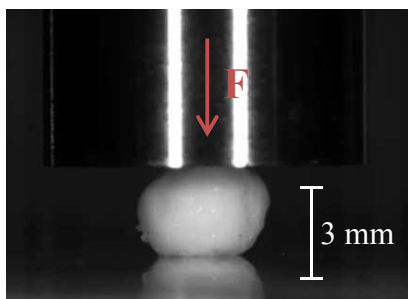

Figure 2: Uniaxial compression test of MCC pellets

Table 1: Results of uniaxial compression tests

Parameter	arithmetic mean ± standard deviation
compression strength / MPa	0.11 ± 0.04
breakage force / N	0.28 ± 0.07
equivalent coefficient of restitution / -	0.31 ± 0.01
stiffness / N mm^{-1}	0.87 ± 0.34

2.2 Simulation Method

The Discrete Element Method (DEM) was introduced in 1979 by Cundall and Strack [6] and is used mainly for simulating particulate systems. In the DEM solid discrete particles which can interact via contact forces F_c are modelled. These particles are assumed to be spherical and indestructible. For each particle the equations of motion (1) and (2) are solved.

$$m_p \frac{dv_p}{dt} = F_g + \sum_i^k F_{c,i} \tag{1}$$

The translational acceleration of a particle p with a mass m_p is calculated from the gravitational force F_g and the contact forces F_c. The contact force is divided into a normal component $F_{c,n}$ and a tangential component $F_{c,t}$ relative to the direction of the interaction. With the moments M_p acting on a particle, that are induced by the tangential components of the contact force, the rotational acceleration can be calculated.

$$J_p \frac{d\omega_p}{dt} = \sum_i^k M_{p,i} \tag{2}$$

The contact forces F_c needs to be modelled using an appropriate contact model. The performed compression tests showed that the pellets used have a dominantly plastic material behavior, which can be good predicted by the model of Walton and Braun [7], [8]:

$$F_{c,n} = - \begin{cases} K_1 \cdot \delta_n & \text{if } K_1 \cdot \delta_n < K_2 \cdot (\delta_n - \delta_0) \\ K_2 \cdot (\delta_n - \delta_0) & \text{if } \delta_n > \delta_0 \\ 0 & \text{if } \delta_n \leq \delta_0 \end{cases} \tag{3}$$

As can be seen in Figure 3 (left), the slope of the curve in the unloading case K_2 is greater than the slope in the loading case K_1. This allows modeling the large plastic deformations δ_0 obtained by the uniaxial compression tests (Figure 3 right).
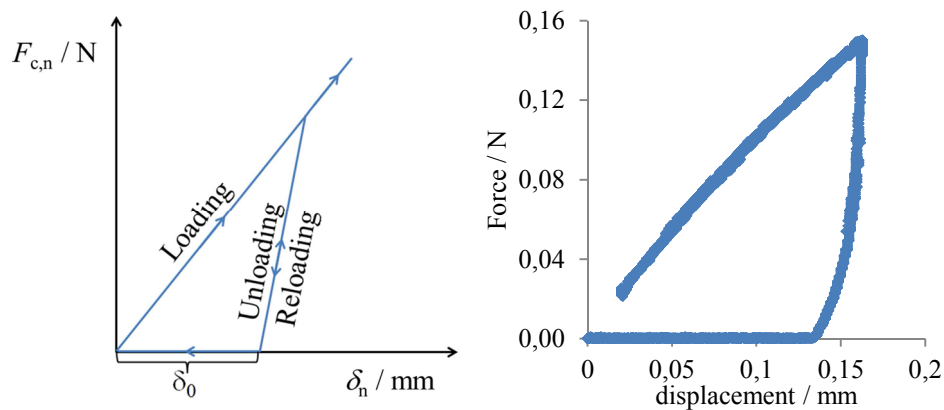
Figure 3: Force-displacement curve of the model of Walton and Braun (left) and experimental results (right)

The model considers the energy loss due to inelastic impact with a constant restitution coefficient e. Based on the restitution coefficient the stiffness of the unloading case can be calculated from the stiffness of the loading case [9]:

$$e = \sqrt{\frac{K_1}{K_2}} \tag{4}$$

Due to the nearly linear force-displacement curves, obtained by the uniaxial compression tests (Figure 3 right) the energy dissipation can be modelled only by the ratio between the stiffness of the loading and unloading case. Additionally, a viscous term is included to prevent possible un-damped low amplitude oscillations [8], [9]. For the numerical simulations the DEM software EDEM (DEM Solutions, UK) was used.

3 RESULTS AND DISCUSSION

The use of a cylindrical coordinate system instead of a Cartesian coordinate system is expedient, because the particle motion in the spheronizer is rotationally symmetric. Thus the spatial distribution of various time-averaged parameters can be displayed by discretizing the poloidal cut (rz-plane). In the evaluation of the collision characteristics, a distinction is made between interparticle collisions, collisions with the friction plate, and collisions with the spheronizer wall. All time-averaged distributions are calculated for the steady state, which was reached after a time of about t = 0.8 s.

3.1 Particle dynamics in the spheronizer

In this section the simulation results of a spheronizer loaded with m = 600 g of particles with a radius of r_p = 2 mm at a rotational speed of the friction plate of n = 1000 rpm are presented. The geometry used in the simulation corresponds to the physical dimensions of the spheronizer used for the experiments having a cross hatched friction plate (see Figure 1) with a diameter of d = 300 mm.
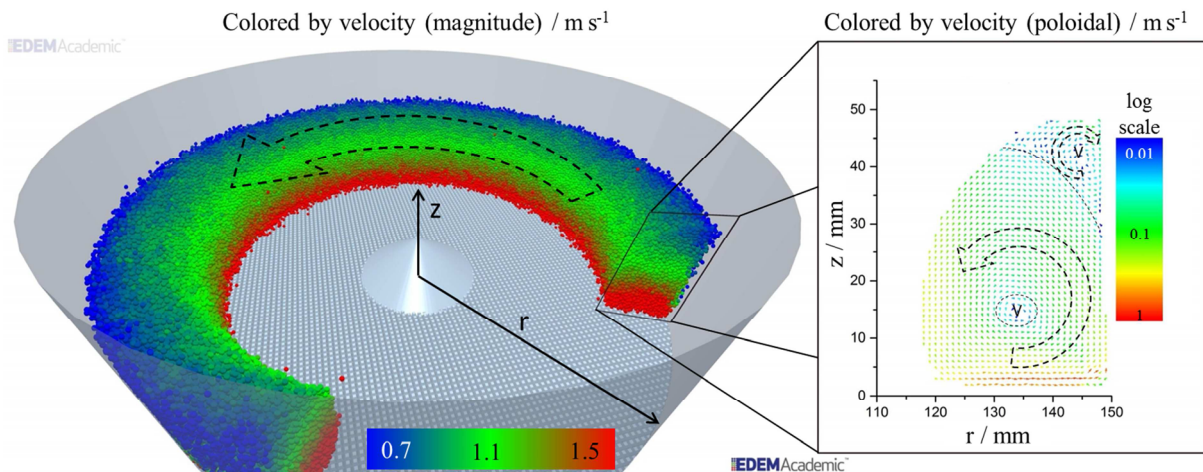

Figure 4: Particle velocities in the spheronizer at n =1000 rpm and m = 600 g

The evaluation of the particle velocities exhibits rotational movements in poloidal direction superimposing the toroidal particle motion as shown in Figure 4. Koester et al. [4] describe five different zones of the particle movements in the poloidal cut. They found two zones V in which the mixing is limited due to the small poloidal velocities. The simulations performed in our work agree with these results. In addition they exhibit a counter-rotating movement in the upper zone V compared with the primary rotational movement (see Figure 4).

Figure 5 shows the time-averaged poloidal velocity field colored by toroidal velocities. As can be seen, the pellets have the greatest toroidal velocities immediately above the friction plate in the outer region. With increasing distance from the friction plate, the average toroidal velocities decrease. The lowest toroidal velocities occur in the upper region of the particle torus near the wall. The comparison of Figure 4 and Figure 5 shows that the velocities of the toroidal movement are significantly greater than that in the poloidal direction. The spatial distribution of the particle residence probability in the poloidal cut can be seen in Figure 6. Local maxima of the particle residence probability occur at regular intervals from the wall. From simulations with different particle sizes a correlation between the intervals of the maxima and the particle size was found. The first maximum is located at a distance which approximately corresponds to the particle radius r_p. The further maxima with decreasing intensity roughly occur at distances of odd multiples of the particle radius. Furthermore, Figure 6 shows a decrease in the particle residence probability near the friction plate with a local maximum at a distance of approximately r_p that is significantly smaller than the radial maxima. Moreover there is a significant increase in the intensity where it intersects the outer radial maximum.
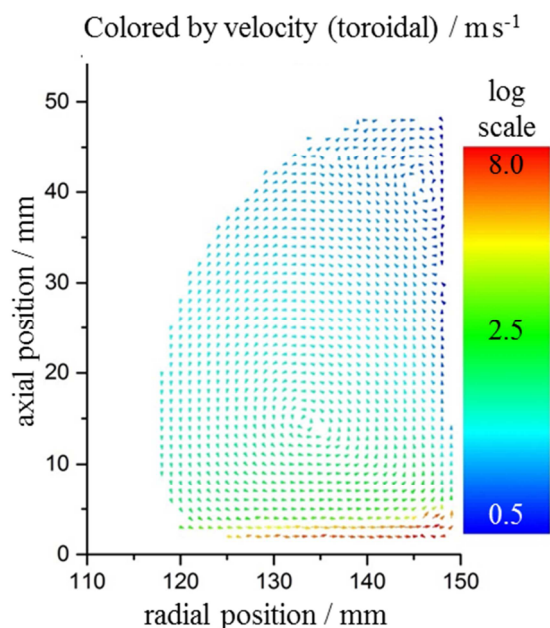

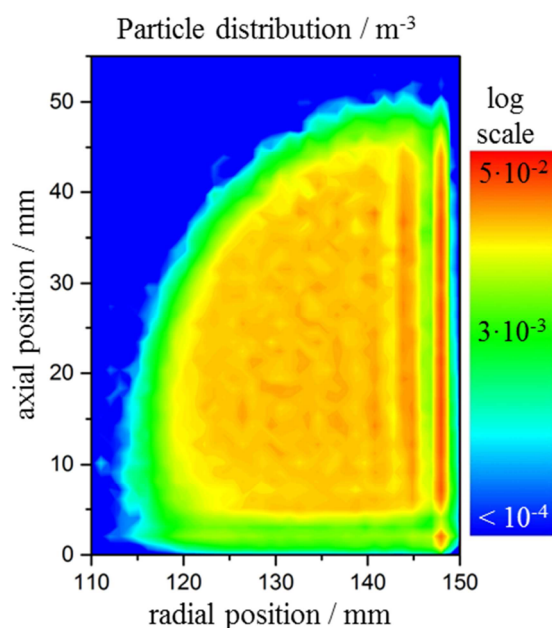**Figure 5**: Time-averaged poloidal velocity field colored by toroidal velocities

Figure 6: Particle residence probability in poloidal cut

In addition to the spatial distribution of the particle residence probability in the spheronizer and the velocity fields, the interparticle collisions and the collisions with the friction plate and the wall are analyzed. The obtained interparticle collision rate is defined as the number of collisions per particle and second within a defined volume of the spheronizer:

$$\dot{N}_{c,p} = \frac{2 \cdot N_{c,p}}{(z_i - z_{i-1}) \cdot \pi \cdot (r_i^2 - r_{i-1}^2) \cdot \Delta t \cdot N_{p,ges}}$$ (5)

The particle geometry collision rate is defined as the number of collision per particle and second within a defined area of the wall or the friction plate:

$$\dot{N}_{c,f} = \frac{N_{c,f}}{\pi \cdot (r_i^2 - r_{i-1}^2) \cdot \Delta t \cdot N_{p,ges}}$$ (6)

$$\dot{N}_{c,w} = \frac{N_{c,w}}{(z_i - z_{i-1}) \cdot r_a \cdot \Delta t \cdot N_{p,ges}}$$ (7)

The axial coordinate z_i as well as the radial coordinate r_i are discretized in 1 mm elements. Figure 7 shows the spatial distribution of the average interparticle collision rate. It can be seen that the greatest values are reached in a lower region near the wall. The collision rate of the particle-friction plate and particle-wall interactions is shown in Figure 8. Overall, the rate of the collisions with the friction plate is an order of magnitude greater than that with the wall. It is remarkable that there is a significant increase of the values in the outer region of the friction plate and the lower region of the wall. Furthermore, the average collision forces are evaluated. The distribution of the interparticle collision forces is shown in Figure 9. It is apparent that the average collision forces are increasing with decreasing distance to the wall and the friction plate. The greatest interparticle collision forces occur immediately above the friction plate. Looking at the average forces of the particle-wall collisions in Figure 10, it can be seen that there is a maximum at a distance to the friction plate of about one particle diameter. Moreover Figure 10 shows that the decrease of the average collision forces with the distance to the friction plate can be described by a power law. The average collision forces of the particle friction plate interactions exhibit a small but characteristic maximum in the outer region. Due to a structured surface of the friction plate the mean collision rate curve shows a high fluctuation.
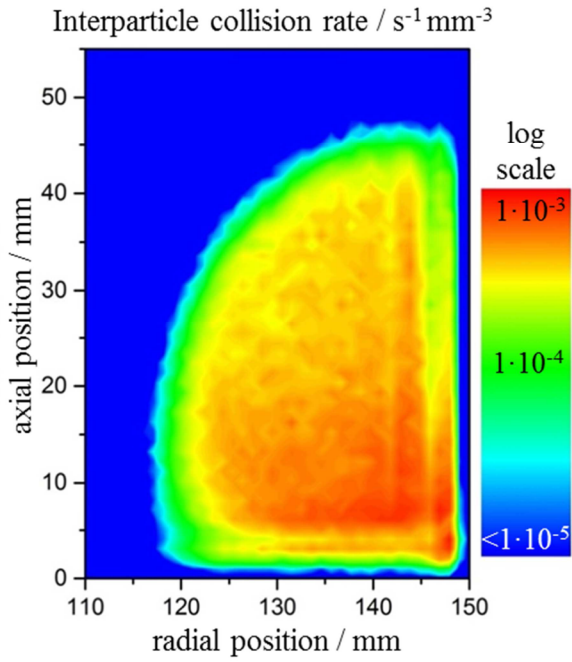
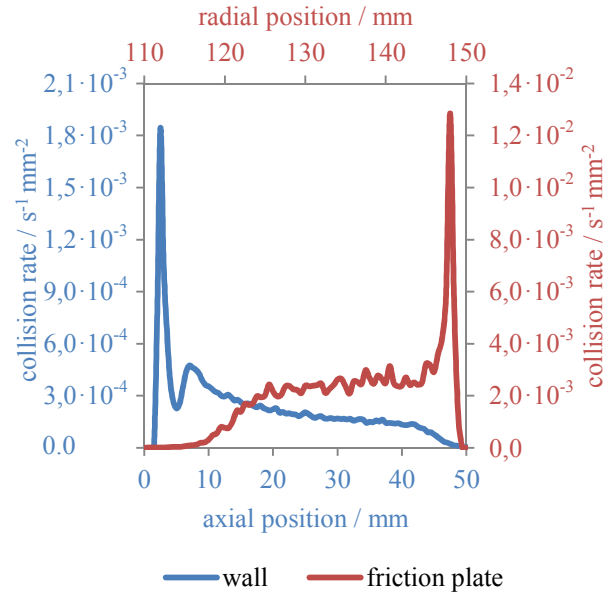**Figure 7**: Rate of the interparticle collisions in poloidal cut

Figure 8: Rate of the collisions with the friction plate and the spheronizer wall
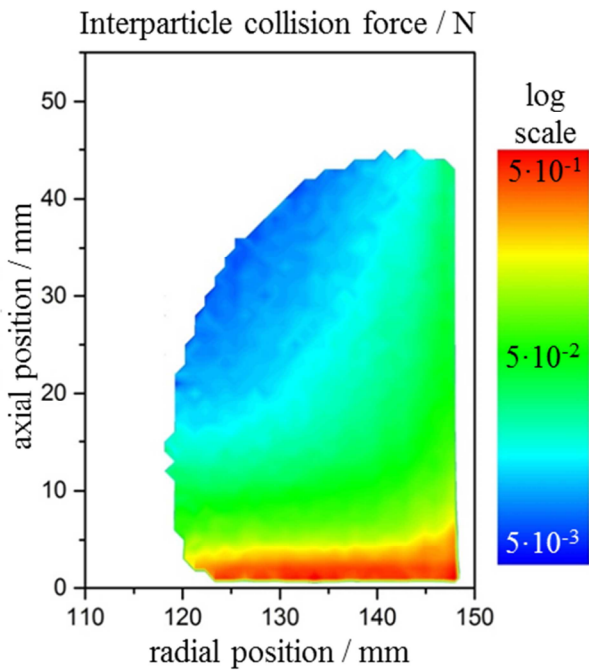

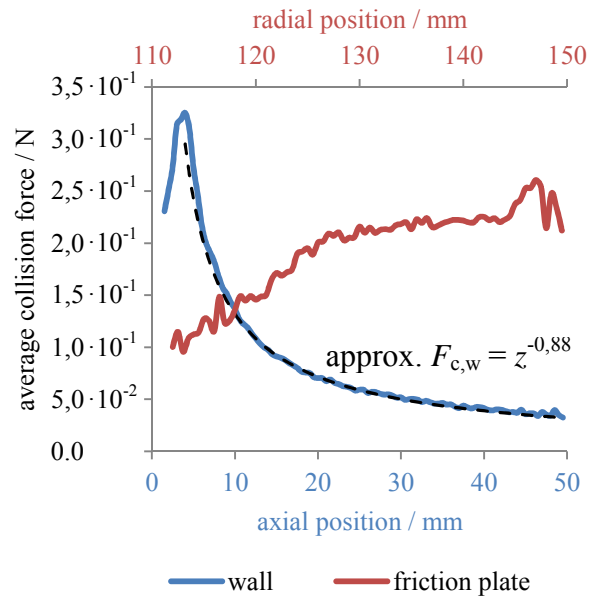**Figure 9**: Average force of the interparticle collisions in poloidal cut

Figure 10: Average force of the collisions with the friction plate and the spheronizer wall

3.2 Influence of various factors on the particle dynamics and the collision characteristics

The influence of different factors affecting the particle dynamics and collision characteristics was investigated. For that purpose from the process conditions, the rotational speed of the friction plate (ROT) and the loading of the spheronizer (LOAD) were varied. From the material properties, the influences of the particle size (PS), coefficient of restitution (CoR), stiffness (ST), and coefficient of static friction (CoF) were investigated. The values of the parameters for the reference case (REF) are given in Table 2. Also, the values for the variation of each parameter are shown.

Table 2: Parameters varied in the simulations

Parameter	ROT / rpm	LOAD / g	PS / mm	CoR / -	ST / N mm^{-1}	CoF / -
Reference	1000	600	2.0	0.25	0.8	1.0
+	1500	1200	2.4	0.50	1.6	1.5
-	500	300	0.8	0.10	0.4	0.5

In Table 3 the influence of the process conditions on the shape of the torus can be seen. Moreover, the distribution of the particle velocities in poloidal and toroidal direction, the collision rates, and the collision forces are characterized by arithmetic mean ± standard deviation.

Table 3: Influence of different process conditions on the particle dynamics and collision characteristics

	Parameter	REF	ROT -	ROT +	LOAD -	LOAD +
Velocity	poloidal / m s^{-1}	0.186 ± 0.196	0.147 ± 0.135	0.209 ± 0.236	0.214 ± 0.220	0.164 ± 0.172
	toroidal / m s^{-1}	1.325 ± 0.790	1.166 ± 0.529	1.461 ± 1.092	1.408 ± 0.847	1.209 ± 0.701
Collision rate	$\dot{N}_{c,p}$ / 10^{-4} s mm^{-3}	3.368 ± 2.116	3.096 ± 1.890	3.100 ± 2.020	5.462 ± 4.212	1.820 ± 1.014
	$\dot{N}_{c,f}$ / 10^{-4} s mm^{-2}	18.40 ± 19.04	15.08 ± 11.85	29.70 ± 39.91	23.70 ± 31.47	13.82 ± 8.596
	$\dot{N}_{c,w}$ / 10^{-4} s mm^{-2}	1.859 ± 2.363	1.353 ± 1.549	2.460 ± 4.125	2.934 ± 4.186	1.121 ± 1.094
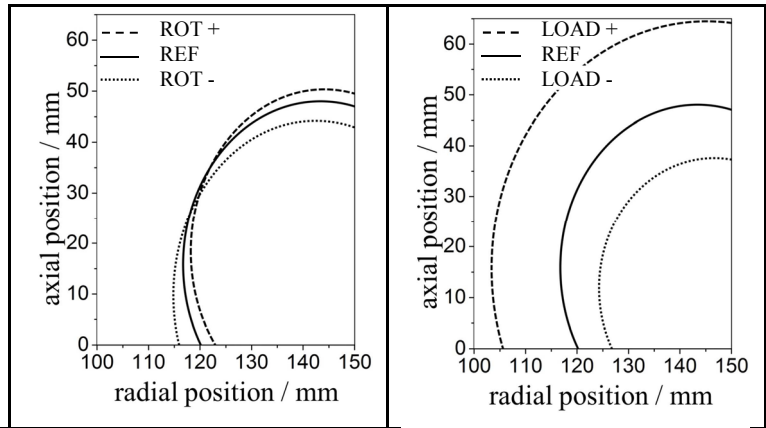
Collision force	$F_{c,p}$ / N	0.052 ± 0.082	0.037 ± 0.047	0.065 ± 0.116	0.059 ± 0.087	0.049 ± 0.081
	$F_{c,f}$ / N	0.217 ± 0.171	0.135 ± 0.100	0.333 ± 0.264	0.200 ± 0.168	0.215 ± 0.163
	$F_{c,w}$ / N	0.138 ± 0.149	0.089 ± 0.081	0.237 ± 0.149	0.131 ± 0.137	0.129 ± 0.133

The shape of the particle torus at different rotational speeds of the friction plate is shown in Table 3. It can be seen that the axial expansion of the torus near the wall is greater and the radial expansion of the torus near the plate is smaller for higher rotational speeds. Furthermore, the poloidal and toroidal velocities increase with the rotational speed. The average collision forces increase with the rotational speed as do the particle-friction plate and particle-wall collision rates. Especially the maxima of the collision rates of the particles with the spheronizer geometry, which can be seen in Figure 8, are increasing. In contrast, the inter-particle collision rate decreases slightly regardless whether the rotational speed is increased or decreased. Different loads of the spheronizer barely affect the shape of the torus. Only the volume of the torus varies. Table 3 shows that the particle velocities and collision rates increase with decreasing loading of the spheronizer. The influence of the loading on the average collision forces is less significant. In addition to the process conditions, Table 4 shows the influence of two particle properties on the particle dynamics and collision characteristics.

Table 4: Influence of different particle properties on the particle dynamics and collision characteristics

	Parameter	REF	PS -	PS +	ST -	ST +
Velocity	poloidal / m s^{-1}	0.186 ± 0.196	0.151 ± 0.153	0.209 ± 0.215	0.184 ± 0.185	0.189 ± 0.204
	toroidal / m s^{-1}	1.325 ± 0.790	1.556 ± 0.801	1.319 ± 0.825	1.404 ± 0.847	1.256 ± 0.732
Collision rate	$\dot{N}_{c,p}$ / 10^{-4} s mm^{-3}	3.368 ± 2.116	8.446 ± 5.022	2.834 ± 1.824	2.976 ± 2.106	3.594 ± 2.374
	$\dot{N}_{c,f}$ / 10^{-4} s mm^{-2}	18.40 ± 19.04	10.09 ± 8.502	23.66 ± 25.20	29.81 ± 26.63	11.22 ± 11.47
	$\dot{N}_{c,w}$ / 10^{-4} s mm^{-2}	1.859 ± 2.363	1.052 ± 0.981	2.258 ± 3.043	1.946 ± 2.797	1.812 ± 1.977
Collision force	$F_{c,p}$ / N	0.052 ± 0.082	0.006 ± 0.011	0.084 ± 0.126	0.043 ± 0.063	0.064 ± 0.107
	$F_{c,f}$ / N	0.217 ± 0.171	0.055 ± 0.039	0.284 ± 0.227	0.149 ± 0.110	0.304 ± 0.257
	$F_{c,w}$ / N	0.138 ± 0.149	0.023 ± 0.025	0.205 ± 0.217	0.110 ± 0.116	0.166 ± 0.176

For a smaller particle size, the torus is getting slimmer and higher. The average poloidal velocity decreases, while the average toroidal velocity increases with decreasing particle size. The average interparticle collision rate decreases with increasing particle size. In contrast, the collision rates of the particles with the spheronizer geometry increase with the particle size. Finally, the influence of the stiffness is analyzed. A smaller stiffness leads to a greater axial expansion of the torus while a larger stiffness causes a wider torus. While the poloidal velocity is barely affected by the stiffness the toroidal velocity increases with the stiffness. The interparticle collision rate increases with the stiffness. In contrast, the collision rates of the particles with the spheronizer geometry increase with decreasing stiffness.

3.3 Comparison of simulation results with PIV measurements

In this section the results of the performed DEM simulation are compared with PIV measurements by Koester et al. [5]. To obtain comparable results, some aspects need to be considered in the evaluation of the simulation data: Firstly, only the particles in an area which is also covered by the high-speed camera [5] should be taken into account (Figure 11). In the upper region of the wall (z > 6 mm) only the outer particles can be considered due to the close packing of the particles. Above the friction plate (z < 6 mm) the camera also captures particles with a greater distance to the wall Δr because of the low particle density (Figure 6). As it can be seen in Figure 11 different distances to the wall were used since it is difficult to assess which is most aptly. Secondly, the camera only captures the axial and circumferential positions of the particles, therefore the radial component of the velocities must not be taken into account. Velocity distributions evaluated in this way are compared with the results of the PIV measurements.
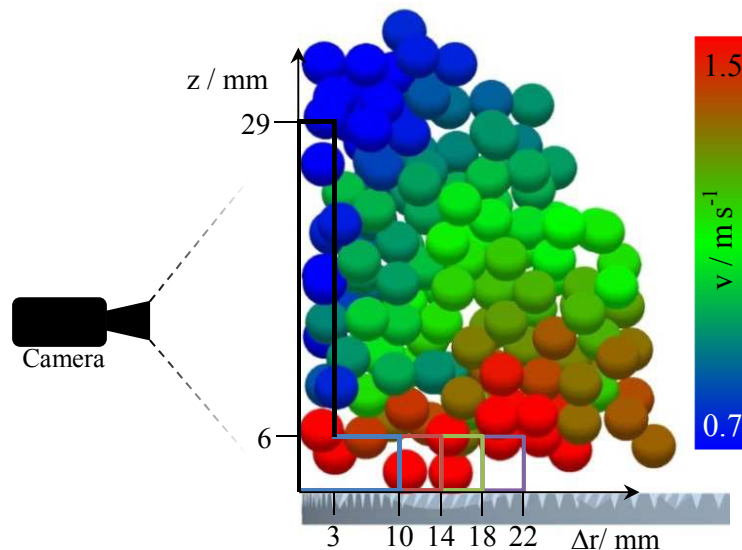

Figure 11: Evaluation of the velocities obtained by DEM for the comparison with the PIV results

In the experiment and simulation the spheronizer consists of a cross hatched friction plate with a diameter of d = 300 mm (Figure 1). Also the process conditions like rotational speed of the friction plate of n = 750 rpm and loading of m = 900 g were the same in the experiment

and simulations. Only the properties of the pellets used for the PIV measurements are not known exactly and may differ from the properties of the pellets tested in this work. Figure 12 shows the particle velocity distribution from the simulation for different areas (Figure 11). Figure 13 shows the averaged particle velocity distribution obtained by Koester et al. [5] in PIV measurements with MCC pellets. Except one modal value at high velocities in the simulation results, the distributions are similar. In the experiments as well as in the simulation there are two modal values at low velocities. These peaks are shifted slightly toward higher values in the simulation results. This difference can be attributed to uncertainties in the particle properties.
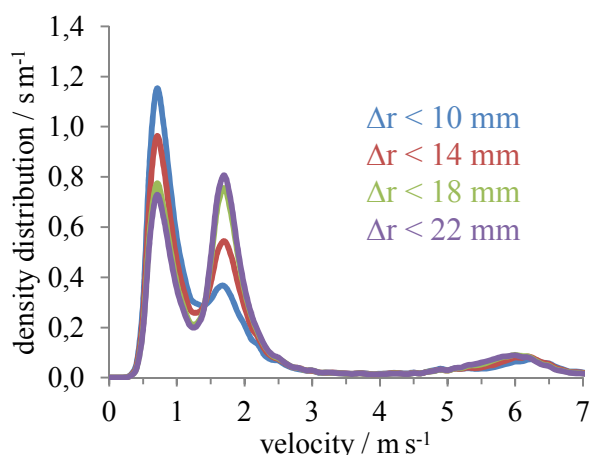

Figure 12: Particle velocity distribution obtained by DEM simulation in different areas
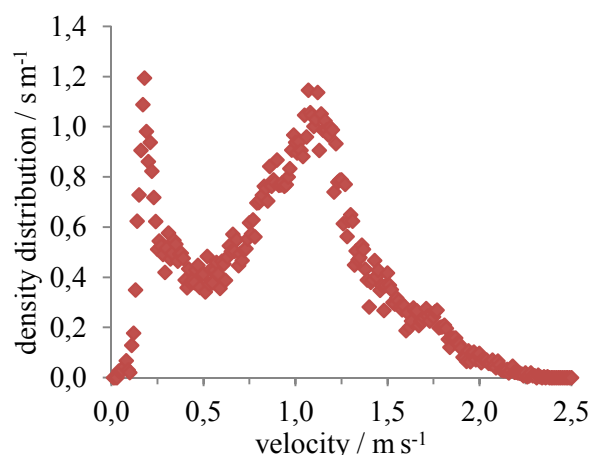
Figure 13: Averaged particle velocity distribution obtained by PIV measurements by Koester [5]

In addition to the PIV measurements with MCC pellets Koester et al. also performed PIV measurements with γ-Al_2O_3 particles [4]. They found a trimodal distribution of the particle velocities. Although pellets of different materials and different process conditions were used, their results are qualitatively similar to the results of the simulation of the present study with three modes each. All in all the comparisons indicate that the DEM simulations can reflect the PIV measurements. To validate this assumption, a consistent set of experiments and simulations needs to be performed with MCC pellets: The particle dynamics in the spheronization process must be measured via PIV and the material properties of the spheronized pellets must be measured immediately. The measured material properties can then be used for the contact model in the DEM simulation of the spheronization process.

4   SUMMARY AND CONCLUSIONS

In this work, the particle dynamics of a spheronization process with MCC pellets was investigated via DEM simulations. The elastic-plastic contact model used in the simulations was calibrated via experiments with spheronized pellets. The average particle movements in the stationary case was displayed as a vector field by spatial discretization of the poloidal cut and time averaging of the particle velocities. The average residence probability of the pellets in the poloidal cut was calculated. Therein local maxima at different radial positions and a decrease near the friction plate were shown. In this area of low residence probability above the friction plate a maximum at a distance of approximately r_p is located. This maximum is

significantly smaller than the radial maxima but exhibits a huge increase where it intersects the outer radial maximum. In addition to the particle residence probability and movements, the collision characteristics were investigated. A maximum in the interparticle and particle-wall collision rates in the lower outer region of the spheronizer was shown. The average collision force also increases with increasing radial and decreasing axial position. Moreover, the influence of different process conditions and material properties was investigated. The influence on the shape of the torus of particles was shown qualitatively. Also the influence on the distribution of the particle velocities, collision rates, and collision forces were determined. The simulation results were compared with results from PIV measurements. Except one modal value at high velocities in the simulation results, the results from PIV measurements with MCC pellets in [5] are similar with 2 modes each at velocities v < 2.5 m/s. Even the results from PIV measurements with γ-Al_2O_3 pellets with different properties in [4] are qualitatively similar because the trimodal distributions also exhibit a modal value at high velocities. To ensure the simulation results can represent the experimental results, further PIV measurements and simulations need to be performed with the same MCC pellets. For these simulations the contact model must be calibrated with the spheronized pellets used in the PIV experiments.

5 ACKNOWLEDGEMENTS

REFERENCES

[1] Koester, M. and Thommes, M. New Insights into the Pelletization Mechanism by Extrusion/Spheronization. *AAPS PharmSciTech* (2010) **11(4)**:1549-1551

[2] Schmidt, C. and Kleinebudde, P. Comparison between a twin-screw extruder and a rotary ring die press. Part II: influence of process variables. *European Journal of Pharmaceutics and Biopharmaceutics* (1998) **45**:173–179

[3] Bouffarda, J., Bertranda, F., Chaoukia, J. and Dumontb, H. Discrete element investigation of flow patterns and segregation in a spheronizer. *Computers and Chemical Engineering* (2013) **49**:170–182.

[4] Koester, M., García, R.E. and Thommes, M. Spheronization process particle kinematics determined by discrete element simulations and particle image velocimentry measurements. *International Journal of Pharmaceutics* (2014) **477:**81–87.

[5] Koester, M. and Thommes, M. Analysis of particle kinematics in spheronization via particle image velocimetry. *European Journal of Pharmaceutics and Biopharmaceutics* (2013) **83**:307–314.

[6] Cundall, P.A. and Strack, O.D. Discrete numerical-model for granular assemblies. *Geotechnique* (1979) **29**:47–65.

[7] Walton, O.R. and Braun, R.L. Stress Calculations for Assemblies of Inelastic Spheres in Uniform Shear. *Acta Mechanica* (1986) **63**:73–86.

[8] DEM Solutions, *EDEM 2.6 Theory Reference Guide* (2014)

[9] Walton, O. *(Linearized) Elastic-Plastic contact model.* Company report, DEM Solutions, (2006).